Emission characterization of externally wetted electrospray thrusters using computed tomography

IEPC-2024-205

David Villegas-Prados[*]
IENAI Space S.L., Leganés, Madrid, 28919, Spain
Plasma & Space Propulsion Team, Universidad Carlos III de Madrid , Leganés, Madrid, 28911, Spain

Justine Kazadi[†]
The University of Liège, Liège, Belgium

Pablo Fajardo[‡]
Plasma & Space Propulsion Team, Universidad Carlos III de Madrid , Leganés, Madrid, 28911, Spain

and

Mick Wijnen[§]
IENAI Space S.L., Leganés, Madrid, 28919, Spain

This study uses computed tomography (CT) to map the current density of an electrospray thruster with an asymmetric emission distribution. The setup includes an angular stage to rotate the thruster and a linear stage to sweep a wire across its active area. Simulations showed that for sufficient resolution, the wire should be 1 mm from the extractor, with 50 angular steps and 300 linear or radial steps. CT scans at various voltages revealed that the northern region began emitting at lower voltages, with more regions emitting consistently as voltage increased from 700 V to 1300 V. However, emissions from nearby beamlets sometimes merged, complicating site extraction. Notably, the southwest region showed inconsistent emission. Scanning electron microscope analysis revealed these non-emitting cones had a damaged, volcano-like shape, likely due to handling errors or manufacturing defects.

Nomenclature

z = wire to extractor distance
N_r = number of radial positions
N_θ = number of angular positions
V_a = applied voltage
I_e = emitted current
I_w = wire current

[*]Ph.D. student, Plasma & Space Propulsion Team, david.villegas@ienai.space, 100329613@alumnos.uc3m.es.
[†]Master student, justine.kazadi@outlook.be
[‡]Full Professor, pfajardo@ing.uc3m.es
[§]Chief Technology Officer, IENAI Space S.L., mick.wijnen@ienai.space

I.   Introduction

Electrospray propulsion systems have gained significant attention in electric propulsion due to their compact size, high specific impulse, and low power consumption. These attributes render them well-suited for micro and nano satellites, offering enhanced efficiency in the low power range (< 100 W) compared to traditional ion or Hall thrusters.[1,2] These systems operate by extracting and accelerating charged particles from a conductive liquid, known as Ionic Liquid (IL). Ionic liquids, with their remarkable stability and negligible vapor pressure at room temperature, are an ideal choice for space applications. The operational principle of electrospray involves an emitter in proximity to an extractor grid. By establishing an electric potential difference between the IL and the extractor grid, ions are extracted from the emitter's tip and accelerated to create a high-speed ion jet, generating thrust.[3]

However, designing electrospray thrusters comes with many challenges. From an operational perspective, the longevity of electrosprays is a critical concern. The primary limiting factor is the overspray from the emitter to the extractor and the subsequent liquid accumulation on the extractor.[4] Overspray is a critical issue within electrospray systems, as the wide plume angles can result in propellant impinging on the extractor, causing problems such as grid shorting, electrode aperture clogging, and propellant back spray.[5] These complications have the potential to ultimately lead to thruster failure.

Successfully addressing overspray as a failure mechanism necessitates a thorough comprehension of plume profiles and emission site characterization. Moreover, variations in flow resistance and tip geometry among emission sites, often arising from the design and manufacturing processes, can lead to non-uniform operational and emission characteristics. This variability may give rise to off-axis emission sites that are not aligned with the extractor grid holes, further intensifying the overspray issue.

Computed tomography (CT) scans serve as a valuable tool for characterizing emission sites and for detecting potential failure mechanisms.[6] CT tomography allows us to infer the emission site operation. This enables the analysis of the thruster's beam profile, identification of off-axis emission sites, inefficient current sharing, and non-uniform emission characteristics. These results can be traced back to the manufacturing processes, allowing us to gain insights into the presence of any defective regions within the emitter and to perform a comprehensive quality assessment of the emitters. Additionally, when CT is conducted over an extended period, it becomes possible to monitor changes in emission characteristics.[6] Such changes may be attributed to emitter degradation or clogging, providing valuable information for ongoing maintenance and performance monitoring.

This paper presents the design, implementation, and testing of a computed tomography scan diagnostic with an externally wetted electrospray thruster from IENAI SPACE. Section II provides background on computed tomography and the approach taken, Section III explains the experimental setup including the thruster employed, Section IV shows the experimental results, and Section V concludes the study.

II.   Methodology and Simulation results

Computed tomography in electrospray thrusters aims to extract the current density distribution, $j(x, y)$, within the thruster plume.[7] This process involves using a wire-probe of width W and length L which is swept radially across the thruster at various angles. If the emission were axisymmetric, sweeping the wire at a single angle would suffice to reconstruct the current density map. However, this ideal scenario is rare, necessitating measurements across a range of radial positions N_r and angular positions N_θ.

Each measurement at a specific radial position r and angle θ represents the line-integrated current density along the wire's length and width, denoted as $j(r, \theta)$. In practice, measurements are continuously obtained over time, resulting in the formation of a matrix $I(r, \theta)$ with discrete values corresponding to N_r and N_θ. The integral expression for the line-integrated current density is given by:

$$I(r, \theta) = \int_L j(x, y) W \, dl \tag{1}$$

The measured projections $I(r, \theta)$ form a sinogram, which is a key component in the process of reconstructing a 2D image. This reconstruction is achieved using the inverse Radon transform, as detailed by.[8] The inverse Radon transform allows for the reconstruction of an object from its projections. Despite the lack of a practical, exact implementation of the inverse Radon transform, several highly effective approximate algorithms have been developed to perform this reconstruction accurately.

The method commonly employed for reconstructing images is the Filtered Back Projection (FBP). This technique involves applying the Fourier transform to the projections, followed by interpolation in Fourier space to obtain the 2D Fourier transform of the image. This transformed image is then inverted to yield the reconstructed image. FBP is one of the fastest methods for performing the inverse Radon transform. The primary tunable parameter in FBP is the filter applied to the Fourier-transformed projections. In this study, a Shepp-Logan filter is used to suppress high-frequency noise in the reconstruction.

Implementing this algorithm is relatively straightforward in MATLAB, which provides a built-in function, *iradon*, for performing the inverse Radon transform. By inputting the sinogram and selecting the desired filter, *iradon* efficiently reconstructs the image using the FBP method.

A.   Simulations

Several simulations were performed to understand the number of angular and linear data points needed, as well as the wire distance required to accurately identify the emission sites in the electrospray thruster. For this purpose, the thruster setup was constructed with each emission site assumed to emit with a Gaussian profile. The width of the profile was based on empirical data of the far plume current distribution. A random generator was implemented to ensure that not all cones emitted uniformly, introducing variations in the emitted current per cone.

Once the random emission profile was generated, the algorithm passed a wire at a specified distance z from the tip of the cone, at various positions (r, θ), to reconstruct the sinogram. The Radon transform was then applied to the sinogram to obtain the computed tomography scan.

Figure 2 illustrates the reconstructed image for fixed values of $N_\theta = 50$ and $N_r = 300$, and for different wire distances $z = 0.5, 1, 1.5$ mm. Figure 1 shows the reconstructed image for $z = 1$ mm and $N_r = 300$, with varying N_θ.
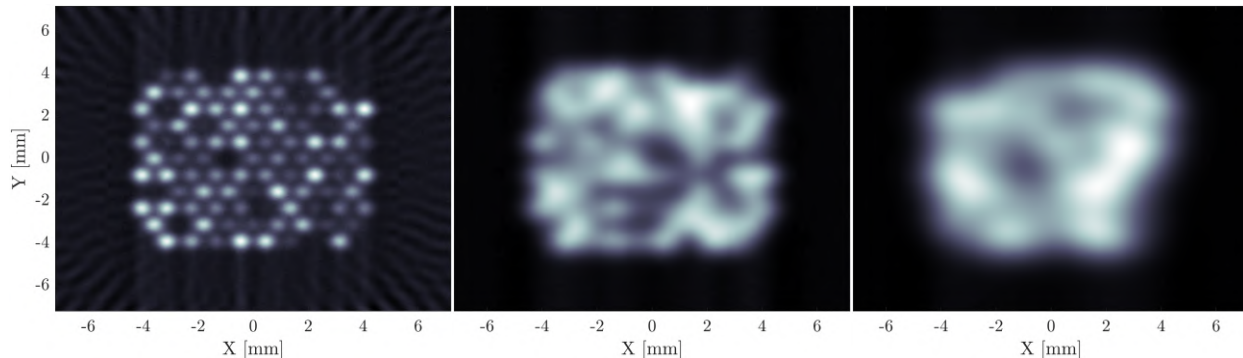
Figure 1: Simulated computed tomography for $N_\theta = 50$ and $N_r = 300$, and for different wire distances, $z = 0.5, 1, 1.5$ mm.

Ideally, the wire should be swept as close as possible to the extractor to identify each individual emission site. As the wire distance increases, the individual beamlets merge, making it difficult to differentiate between emission sites. Therefore, placing the wire as close as possible to the extractor is crucial.

Regarding the number of angular and linear steps, N_r is fixed by the amount of data points obtainable in a single sweep. On the other hand, different values of N_θ have been simulated for the case where $z = 1$ mm and $N_r = 300$. It was observed that with $N_\theta = 10$, the 2D map is quite noisy, and the quality improves as N_θ is increased. The drawback of increasing the number of angular steps is the increased time required to complete the entire test. However, this dataset represents a perfectly created emission scenario, whereas in reality, even with a high number of steps and close wire distance, emissions may still exhibit noise.

The parameters chosen for the test are $z = 1$ mm, $N_r = 300$, and $N_\theta = 50$.
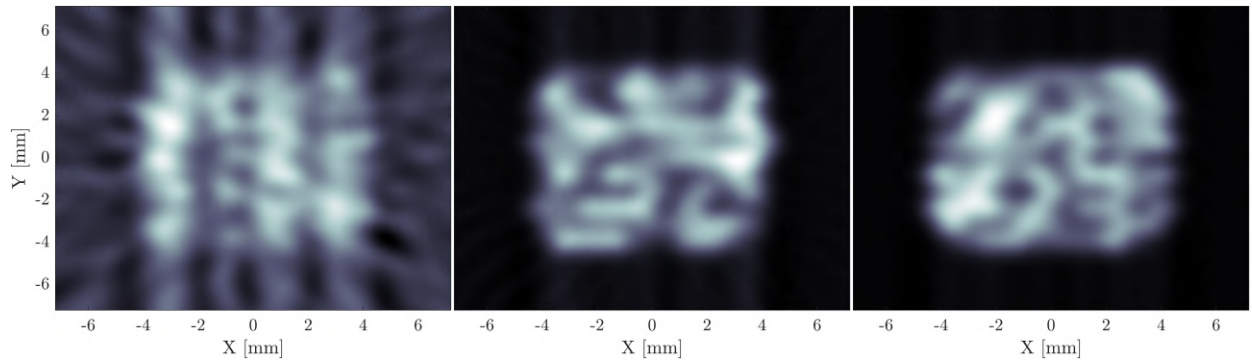
Figure 2: Simulated computed tomography for $z = 50$ and $N_r = 300$, and for different angular steps, $N_\theta = 10, 30, 50$

III. Experimental methods

A. Thruster description

The electrospray thrusters used in this study[9] consist of an borosilicate-based extractor grid and an oxidized, silicon-based externally wetted emitter array, featuring 101 micro cones with nano-texturization to control the hydraulic resistance and a propellant reservoir for liquid storage. In addition, the emitter includes multiple feeding holes that allow the ionic liquid to flow passively from the reservoir positioned beneath the emitter to the emission sites. To ensure an uninterrupted liquid connection between the emitter and reservoir, a porous textile material is inserted. The reservoir itself is constructed using 3D printing technology, employing a porous aluminum piece. A schematic of a single micro-cone is shown in Figure 3. The ionic liquid used in this work is 1-Ethyl-3-methyl-imidazolium bis-trifluoromethylsulfonyl-imide, also known as EMI-Im or EMI-NTf2 in the literature. Ionic liquids are room temperature molten salts composed of positively charged cations and negatively charged anions.
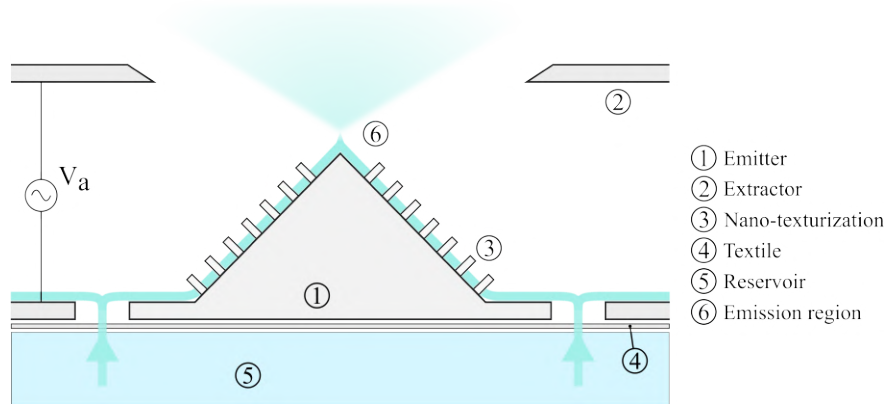
Figure 3: Schematic of externally wetted emitted with nano-texturization for impedance control (not to scale), featuring emitter, extractor grid and reservoir.

B. Computed tomography setup

To perform tomography measurements, we utilized linear and rotary stages, specifically the X-LSM50A-SV2 and X-RSW60A-SV2 models from Zaber, which are vacuum-rated. The linear stage is equipped with a manual vertical stage mounted atop its sliding platform. This vertical stage is used to place the wire at the desired distance from the extractor grid and it has mounted a custom "handsaw" metal piece that houses a printed circuit board (PCB) for establishing the electrical connection to the wire. At one extremity of the handsaw plate, a tensioning mechanism is incorporated to ensure the wire remains taut. The wire connects to

the PCB via a screw, and SMA makes the connection with air-side. Movement of the linear stage facilitates the necessary linear measurements by displacing the wire accordingly.

Conversely, the rotary stage supports the thruster, with its electrical connections facilitated through a liquid connector housed within a borehole at the center of the rotary stage. This liquid connector is affixed to a PCB with a screw, enabling seamless electrical connectivity to the thruster. This configuration permits unobstructed rotation of the thruster without the risk of cable entanglement. Figure 4 presents a CAD rendering of the computed tomography setup alongside an actual image of the thruster positioned within the setup.

Due to assembly constraints, the extractor grid is positioned 0.5 mm below the top part of the assembly holder. Adding this distance to the cone tip-to-extractor distance of 0.1 mm results in a minimum distance of 0.6 mm. To ensure a margin of 0.4 mm from the assembly and to avoid wire breakage, the wire distance was set to 1 mm. The wire, made of tungsten, has a diameter of 25 μm.

On the air-side, the wire current connection is linked to a transimpedance amplifier (TIA) with a 1 MΩ gain. The thruster is operated using a high-voltage (HV) amplifier. A dedicated software system ensures synchronization between the stage movements and thruster operation.

The thruster is operated using a HV amplifier
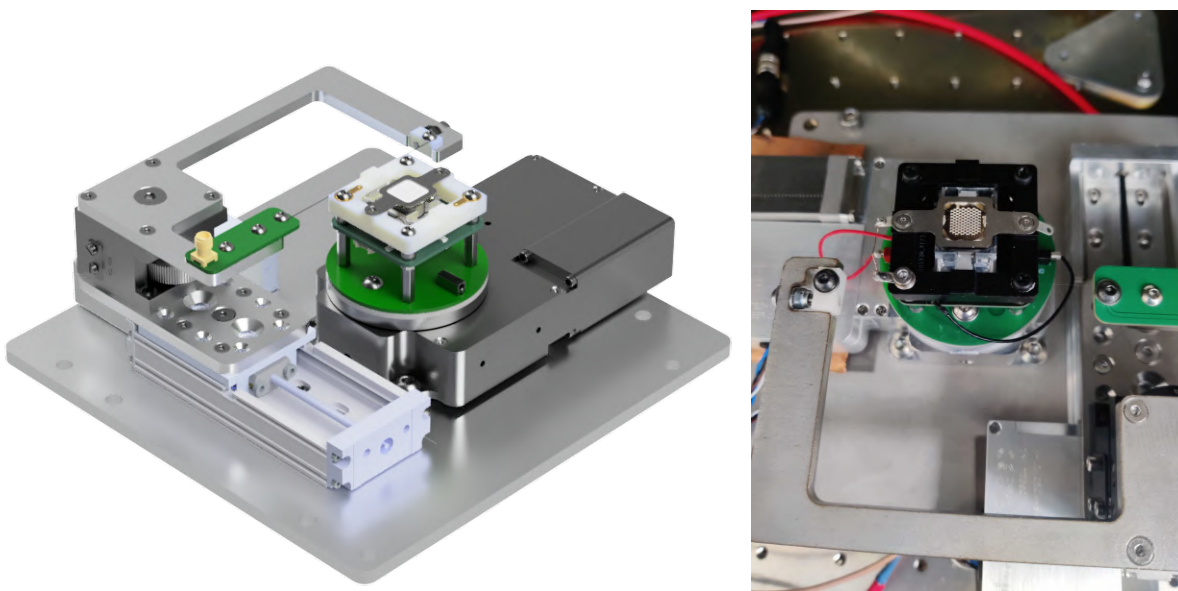
Figure 4: CAD of tomography assembly and actual image of the thruster mounted on top of the tomography setup.

C.   Vacuum facilities

The tests were conducted at the IENAI SPACE facilities located in Leganés, Madrid, Spain. The vacuum facility features a cylindrical chamber with an 800 mm diameter and a length of 1000 mm, extended to a maximum length of 1200 mm due to its curved ends. This chamber includes a retractable plate with mounting holes for securing the experimental setup. The chamber pressure is maintained at 10^{-6} mbar throughout the tests by an Edwards 400 nEXT turbo-molecular pump. Figure 5 depicts the chamber housing the computed tomography experiment and the thruster.
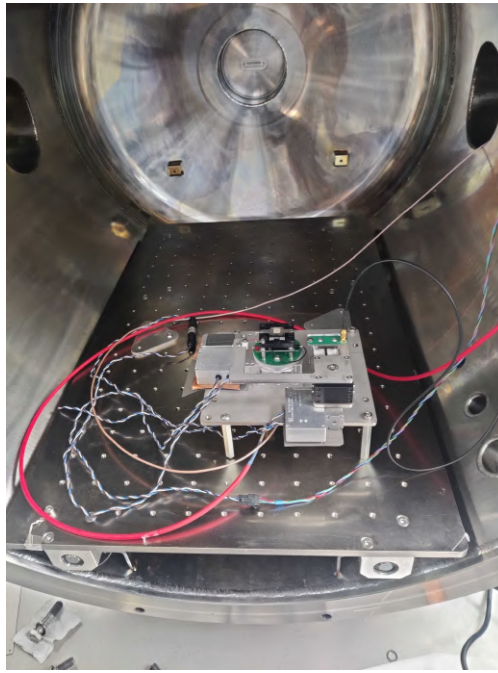
Figure 5: Vacuum chamber and computed tomography setup with electrospray thruster and connections before the start of the test.

D. Operation procedure

To achieve high-resolution computed tomography, we have determined that numerous linear and angular steps are required. Ideally, a rapid snapshot of the current is desired; however, in practice, the tomography process is time-consuming, and the thruster's dynamics may change over this period. To optimize time efficiency, the linear stage moves across the thruster during the high-voltage on-state at a sufficiently low speed to capture an adequate number of data points. This is synchronized such that the linear stage moves forward when the emission is negative and the thruster moves backward when the emission is positive. Upon completing a cycle, the voltage ramping time is utilized to adjust the angular stage to the next angle. This method ensures data collection at fixed angular steps, with the linear stage sweeping to obtain the wire current distribution $I_w(x)$ along the axial direction. This process is repeated for all angles.

This process is conducted at seven operational voltages ranging from 700 V to 1300 V, in increments of 100 V. The synchronization details are illustrated using the data for $V_a = 1100$ V, which includes the applied voltage, emitted current, wire current, and both angular and linear positions, as shown in Figure 6. A close-up of one cycle is depicted in Figure 7.

The high-voltage (HV) trapezoidal waveform features a 30-second HV period with 6-second ramps, resulting in a total duration of 1 minute and 24 seconds per angle. With $N_\theta = 50$, the overall test duration is 70 minutes. Ensuring the thruster's steady operation throughout this period is critical. The emitted current data, presented in the figure, confirms that the current remained constant throughout all the tests.
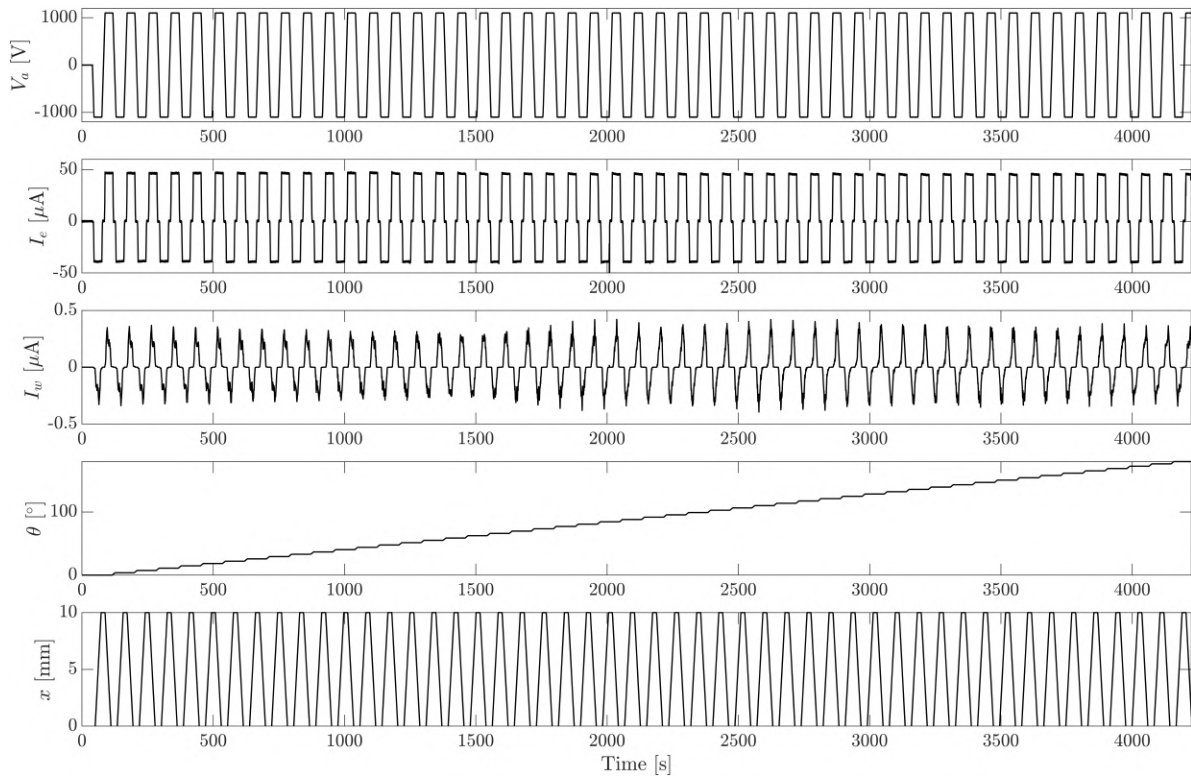
Figure 6: Applied voltage, emitted current, collected wire current, and angular and linear movement over time for a whole computed tomography scan at a given voltage.
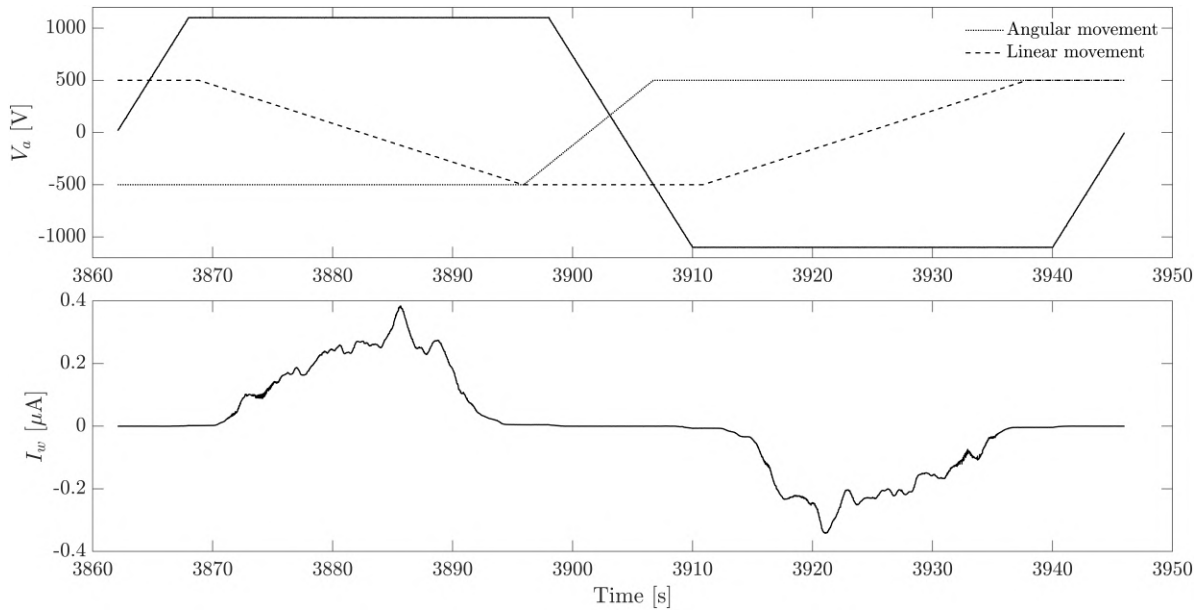
Figure 7: Snapshot of a single cycle showing how the angular and linear movement are synchronized with the applied voltage to obtain the wire current.

IV.   Experimental results

A.   Thruster current-voltage characteristics

The emitted current for a single cycle at each tested voltage is illustrated in Figure 8. Across all cases, the emitted current exhibits stability, albeit showing minor variations in the negative polarity at higher voltages, typically within the range of 1-2 μA. Figure 9 presents the mean emitted currents for all tested voltages, along with their respective standard deviations. Notably, at 1200 V, the maximum deviation is observed with emitted currents of 92 ± 1.6 μA and -79 ± 2.3 μA, respectively. The first test at 700 V was performed close to the onset of emission, currents were recorded as $+1.5 \pm 0.3$ μA and -1.2 ± 0.3 μA, and this case will help highlighting the initial emission sites.
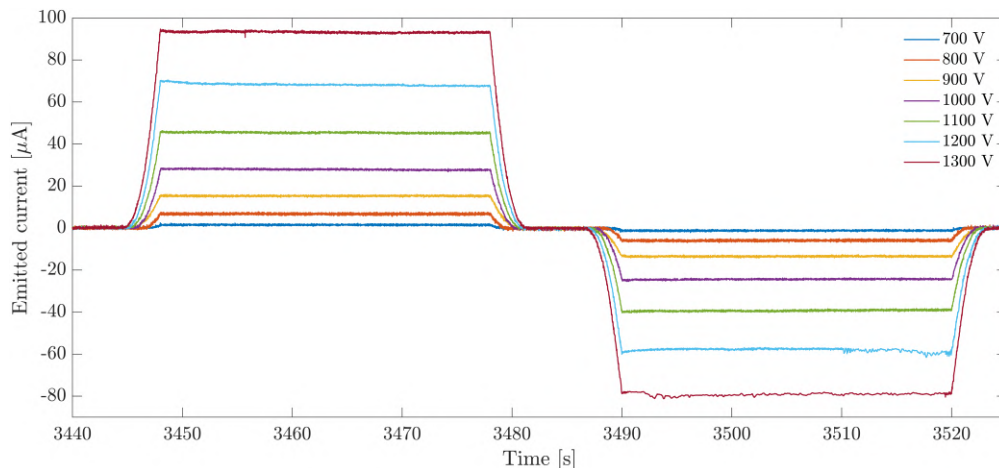
Figure 8: Snapshot of emitted current cycle for the different voltage cases tested.
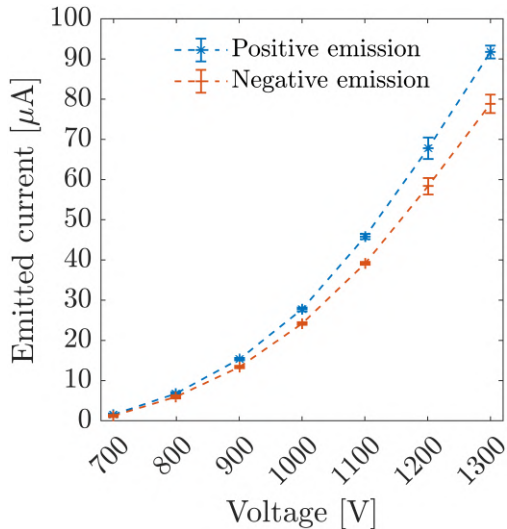
Figure 9: Current-voltage curve for positive and negative emission with standard deviation bars.

B.   Computed tomography current maps

For all the reconstructed tomography maps, the cone-to-wire distance was set to 1 mm, the number of angular steps is $N_\theta = 50$, and the linear stage is swept at roughly 0.3 mm/s, corresponding to $N_r = 300$ in post-processing. Despite the stages having an extremely high step resolution of 20 μm, the primary limiting factor remains the data collection rate across all devices.

In Figure 10, the CT scan for positive emission is shown on the left and for negative emission on the right, with increasing applied voltage. The intensity in each image is normalized relative to its own maximum for optimal visualization. To provide clear orientation, the images use a north-south-east-west nomenclature to describe locations within them.

A notable observation is that the emission sites appear identical for both positive and negative polarity voltages across all tested conditions, indicating consistent emission from the same locations regardless of voltage polarity.

At 700 V, initial emission sites are concentrated in the northern part of the emitter, with minimal emission observed in the southern part. The data at this voltage exhibit higher noise levels, and emission sites appear larger compared to other voltage settings. Increasing the voltage to 800 V introduces additional emission sites, primarily located in the northern part of the emitter. By 900 V, emission sites begin to emerge in the southeast region of the emitter. As voltage further increases to 1000 V, the emission pattern becomes more uniform across the emitter, although the southwest region remains inactive with only a few low-intensity emission sites. Similar distributions are observed at 1100 V and 1200 V, with a noticeable absence of emission in a specific region. At 1300 V, sporadic emission is observed in the southwest region, but it remains significantly less pronounced compared to the rest of the emitter.

Additionally, it is noteworthy that the emitter lacks a central cone, which is why no emission is observed in the center of the images across all cases. Besides the non-emitting southwest region, it appears that specific cones do not emit consistently, indicated by regions with significantly reduced or absent intensity.

(a) **700V/1.5µA**
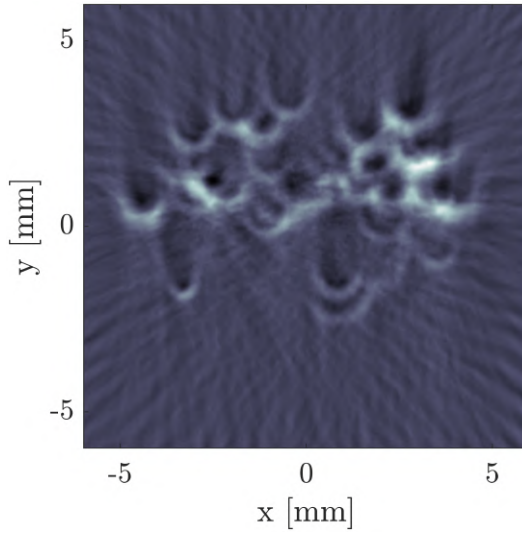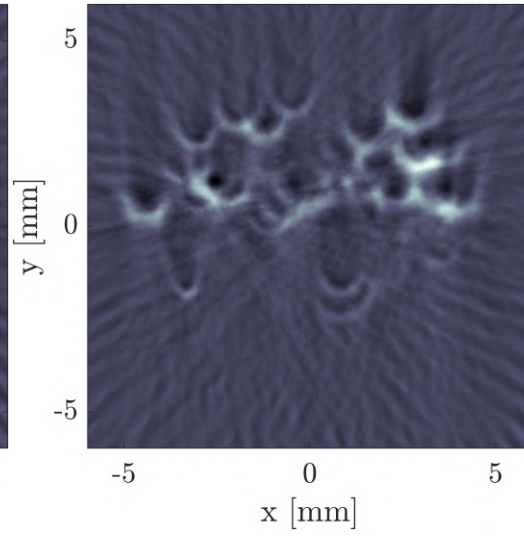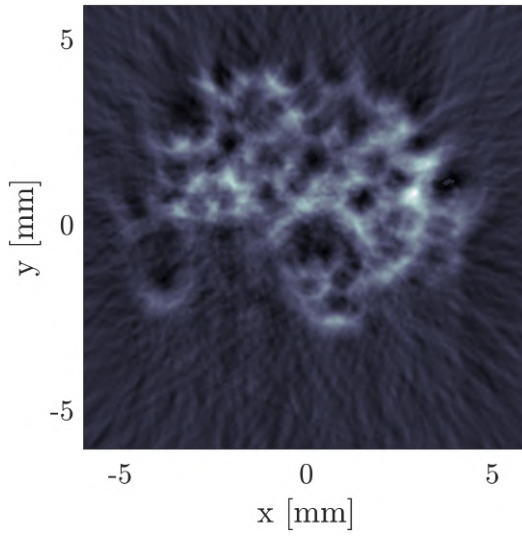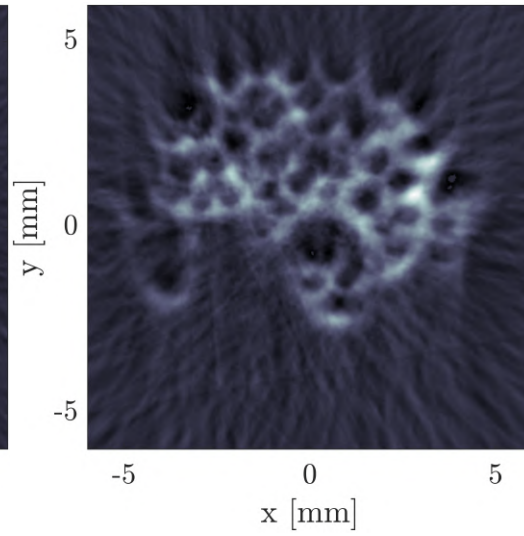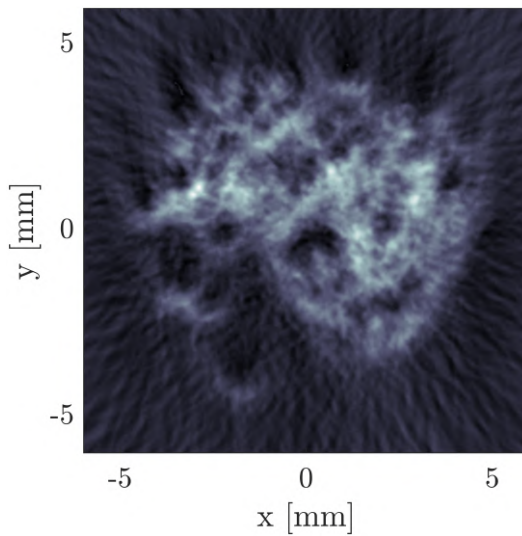
(b) **-700V/-1.2µA**

(c) **800V/6.8µA**

(d) **-800V/-5.9µA**

(e) **900V/15.4µA**

(f) **-900V/-13.4µA**

(a) **1000V/27.8μA**
(b) **-1000V/-24.2μA**
(c) **1100V/45.8μA**
(d) **-1100V/-39.2μA**
(e) **1200V/67.8μA**
(f) **-1200V/-59.4μA**
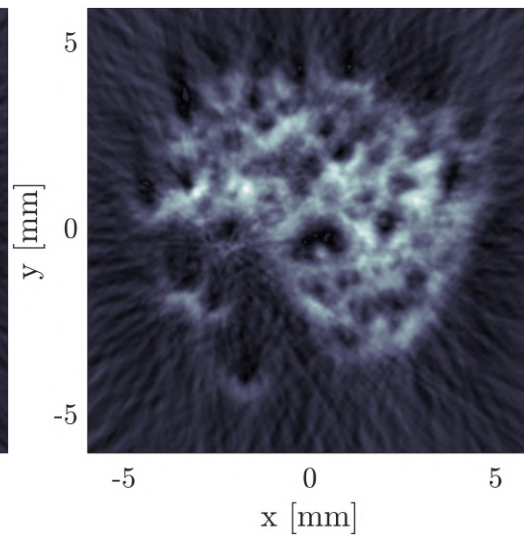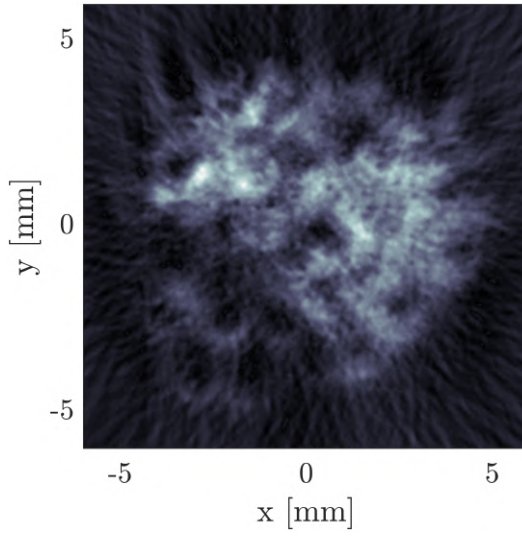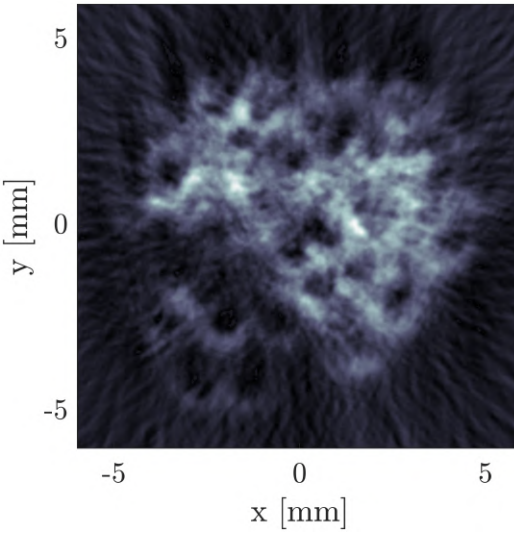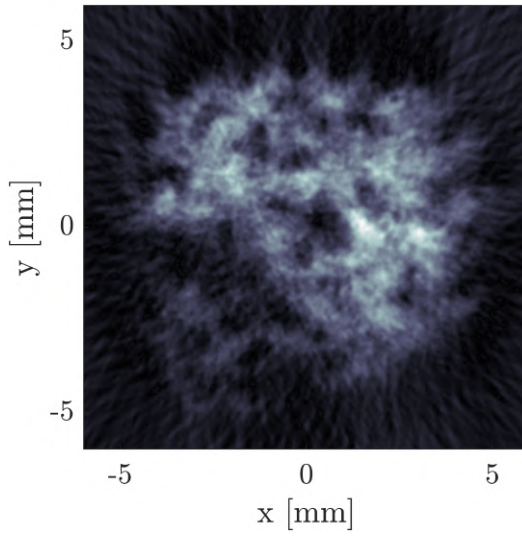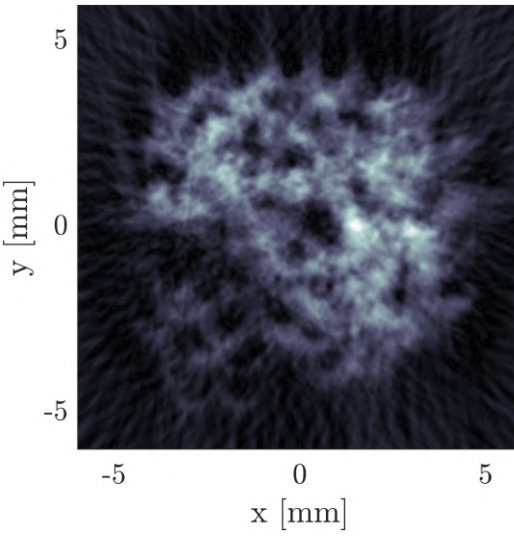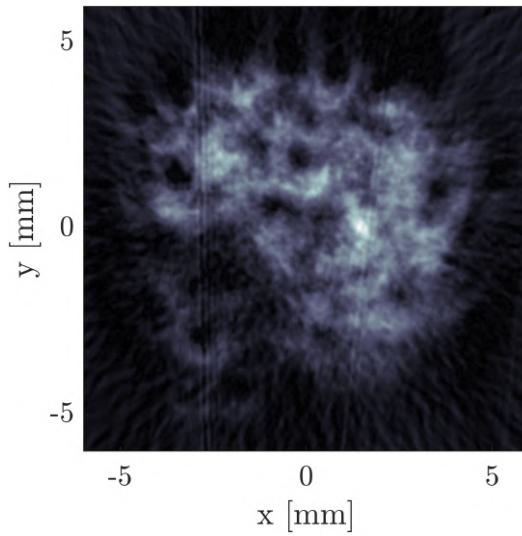
(a) **1300V/91.7μA** (b) **-1300V/-79.8μA**
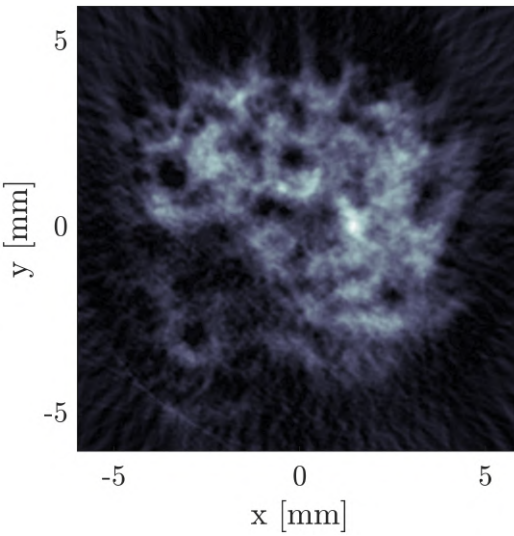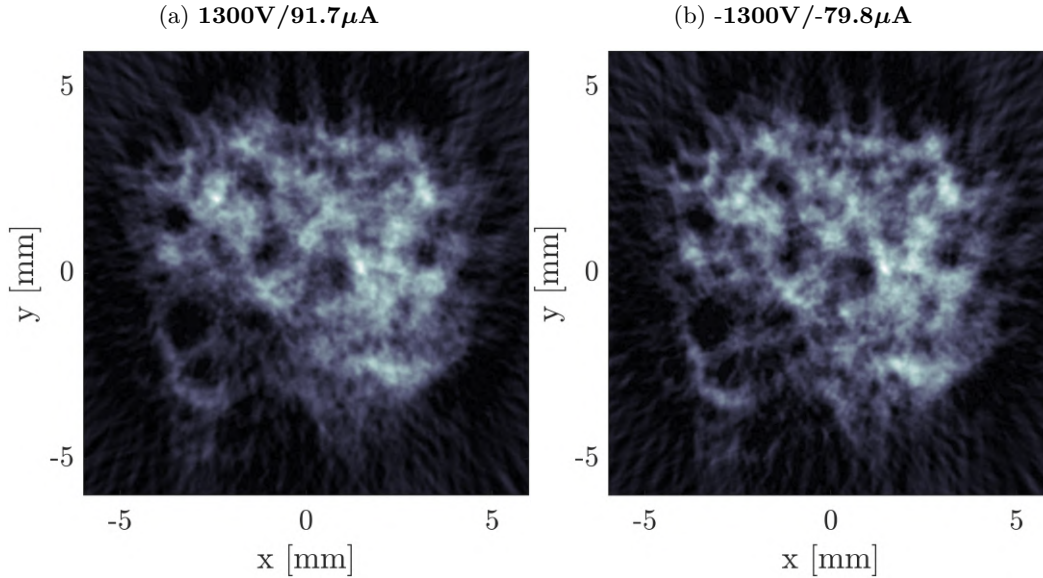
Figure 10: Computed tomography maps at different operating voltages for positive and negative polarity.

C. Scanning electron microscope images

Tomography serves as a crucial diagnostic tool, enabling the characterization of individual emission sites and providing insights into their emission behaviors. However, deriving meaningful conclusions regarding non-emitting regions necessitates aligning CT results with the emitter's fabrication details.

To discern differences among cones in various regions, the emitter was analyzed using a Scanning Electron Microscope (SEM). Imaging was conducted with a FEI Teneo at the Electron Microscopy Unit of Universidad Carlos III de Madrid. Figure 11 displays images from the top of the southwest and northeast quadrants, with Figure 12 providing close-up views of cones in each region.
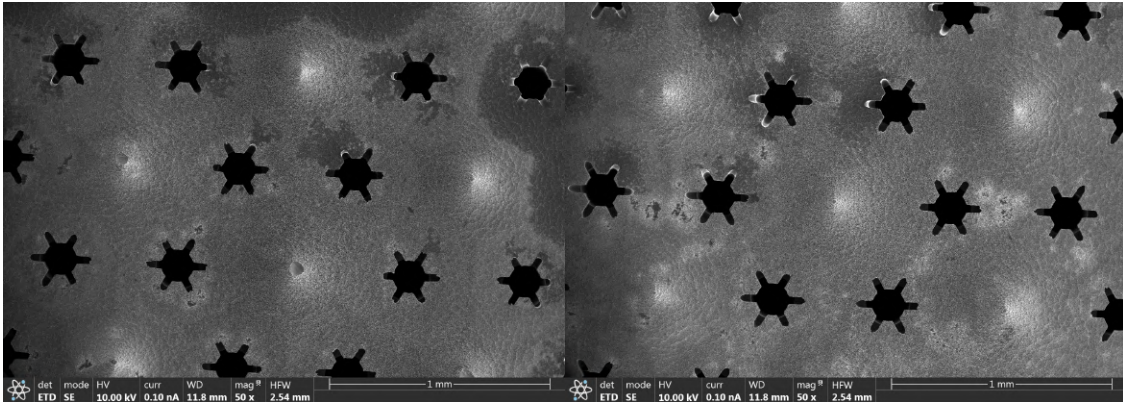
Figure 11: SEM images of southwest and northeast region.

The SEM images reveal that cones in the southwest region do not emit due to tip loss, resulting in a volcano-shaped structure. This observation correlates with the emission map from tomography, highlighting the compromised state of these cones. This particular emitter was exclusively used for testing purposes and has not been utilized subsequently, suggesting that the volcano-shaped cones may have resulted from mishandling during manufacturing or corrosion caused by the ionic liquid. Among these possibilities, mishandling appears most plausible, though further investigation is required for definitive conclusions.

Nevertheless, the potential of tomography in diagnosing emitter issues has been underscored, demonstrating its capability to detect and infer problems affecting emitter performance.
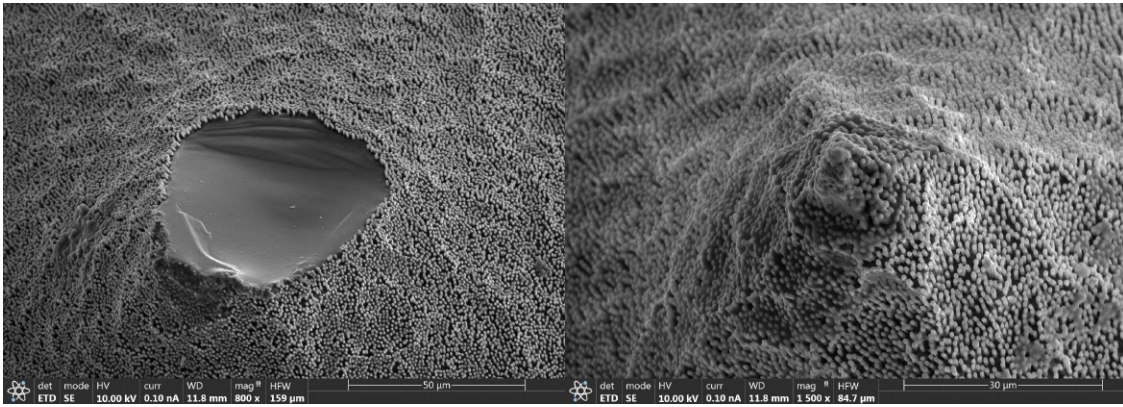
Figure 12: SEM close-up pictures of the cones with volcano shape and normal ones.

V. Conclusion

A computed tomography (CT) method has been developed to reconstruct the current density map of an electrospray thruster with an asymmetric distribution. The setup consists of an angular stage that rotates the thruster and a linear stage that sweeps the wire across the thruster's active area. Simulations indicated that for a CT scan with sufficient resolution to distinguish emission regions, the wire must be positioned 1 mm from the extractor. Furthermore, a large number of angular and linear steps are required for the reconstruction, with $N_\theta = 50$ and $N_r = 300$ in our case. This is primarily due to the compact design of the thrusters at IENAI SPACE, where the distance between cones is 0.8 mm.

A key aspect of computed tomography is ensuring that the thruster operates steadily throughout the test duration. This was confirmed with tests lasting approximately 70 minutes, during which a steady emission was maintained for all tested voltages. Significant effort was also invested in developing synchronization software to enable continuous sweep measurements of positive and negative emissions at different angles.

The computed tomography scans at different voltages show an increase in emission with voltage. The northern region of the emitter starts emitting at lower voltages, and as the voltage increases from 700 V to 1300 V, more regions begin emitting consistently. Emission sites can be extracted from the maps, but this is challenging as emissions from nearby beamlets sometimes merge. A closer wire probe could improve the reconstruction, but improvements in the assembly are needed to allow the wire to be positioned closer to the extractor.

The most notable observation from the maps is the southwest region, which did not show consistent emission despite increasing the voltage, with only a few spots emitting slightly. To verify and understand the reason behind this anomaly, the emitter was examined using a scanning electron microscope. It was found that the non-emitting cones were "eaten away" and had a volcano shape, in contrast to the other cones that maintained their cone-like shape. Several theories can be proposed about the state of these cones, but most converge on the fact that the emitters are extremely fragile, and any error during handling can damage them, as observed in the images.

These measurements constitute the first data we have obtained from computed tomography. Future efforts will focus on improving the setup to achieve closer maps where individual cones can be differentiated. Additionally, it will be interesting to conduct long-term firings where computed tomography is periodically performed to observe how the emission sites change over time. Furthermore, a Faraday probe could be positioned in future experiments to obtain the far plume angular distribution and correlate it with the tomography results.

Acknowledgments

References

[1] K. Lemmer, "Propulsion for cubesats," *Acta Astronautica*, vol. 134, pp. 231–243, 2017.

[2] D. Krejci, M. G. Jenkins, and P. Lozano, "Staging of electric propulsion systems: Enabling an interplanetary cubesat," *Acta Astronautica*, vol. 160, pp. 175–182, 2019.

[3] J. F. d. l. Mora, G. J. Van Berkel, C. G. Enke, R. B. Cole, M. Martinez-Sanchez, and J. B. Fenn, "Electrochemical processes in electrospray ionization mass spectrometry," *Journal of Mass Spectrometry*, vol. 35, no. 8, pp. 939–952, 2000.

[4] N. M. Uchizono, A. L. Collins, A. Thuppul, P. L. Wright, D. Q. Eckhardt, J. Ziemer, and R. E. Wirz, "Emission modes in electrospray thrusters operating with high conductivity ionic liquids," *Aerospace*, vol. 7, no. 10, p. 141, 2020.

[5] A. Thuppul, A. Collins, P. Wright, N. Uchizono, and R. Wirz, "Mass flux and current density distributions of electrospray plumes," *Journal of Applied Physics*, vol. 130, no. 10, 2021.

[6] D. G. Courtney, Z. Wood, and T. Fedkiw, "Reconstructing electrospray plume current spatial distributions using computed tomography," in *36th International Electric Propulsion Conference, University of Vienna, Austria*, pp. 15–20, 2019.

[7] T. Fedkiw, Z. D. Wood, and N. R. Demmons, "Improved computed tomography current mapping of electrospray thrusters," in *AIAA Propulsion and Energy 2021 Forum*, p. 3389, 2021.

[8] A. C. Kak and M. Slaney, *Principles of computerized tomographic imaging*. SIAM, 2001.

[9] D. Villegas-Prados, J. Cruz, M. Wijnen, S. Correyero, P. Fajardo, and J. Navarro-Cavallé, "Impact of propellant temperature on the emission regime of an externally wetted electrospray system using time-of-flight mass spectrometry," *Acta Astronautica*, vol. 213, pp. 145–155, 2023.